

ViPOcc: Leveraging Visual Priors from Vision Foundation Models for Single-View 3D Occupancy Prediction

Yi Feng¹, Yu Han², Xijing Zhang¹, Tanghui Li¹, Yanting Zhang², Rui Fan^{1*}
¹Tongji University,
²Donghua University
 {fengyi, rui.fan}@ieee.org

Abstract

Inferring the 3D structure of a scene from a single image is an ill-posed and challenging problem in the field of vision-centric autonomous driving. Existing methods usually employ neural radiance fields to produce voxelized 3D occupancy, lacking instance-level semantic reasoning and temporal photometric consistency. In this paper, we propose ViPOcc, which leverages the visual priors from vision foundation models (VFMs) for fine-grained 3D occupancy prediction. Unlike previous works that solely employ volume rendering for RGB and depth image reconstruction, we introduce a metric depth estimation branch, in which an inverse depth alignment module is proposed to bridge the domain gap in depth distribution between VFM predictions and the ground truth. The recovered metric depth is then utilized in temporal photometric alignment and spatial geometric alignment to ensure accurate and consistent 3D occupancy prediction. Additionally, we also propose a semantic-guided non-overlapping Gaussian mixture sampler for efficient, instance-aware ray sampling, which addresses the redundant and imbalanced sampling issue that still exists in previous state-of-the-art methods. Extensive experiments demonstrate the superior performance of ViPOcc in both 3D occupancy prediction and depth estimation tasks on the KITTI-360 and KITTI Raw datasets. Our code is available at: <https://mias.group/ViPOcc>.

1. Introduction

As a key ingredient of environmental perception in autonomous driving, 3D occupancy prediction has garnered considerable attention in recent years [2, 13, 27, 31]. Early efforts tackle this problem through supervised learning, which requires extensive 3D human-labeled annotations and depth ground truth acquired using additional range sen-

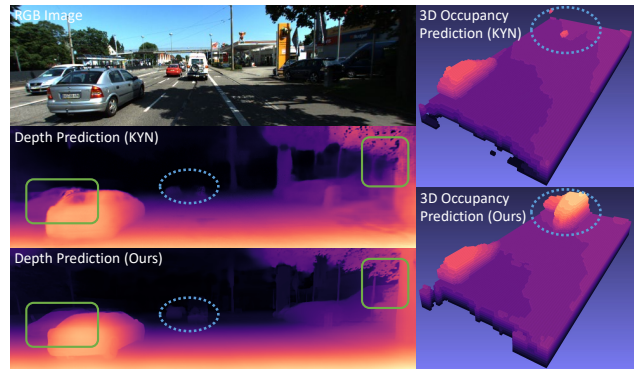


Figure 1. **Single-view 3D scene reconstruction results.** KYN [18] struggles to recover clear object boundaries (green boxes) and exhibits poor reconstruction performance for distant objects (blue circles). ViPOcc outperforms KYN in both monocular depth estimation and 3D occupancy prediction tasks.

sors [12]. More recently, neural radiance field (NeRF)-based approaches have emerged as promising techniques for unsupervised single-view 3D occupancy prediction [18, 32], noted for their capability to render photorealistic images from novel viewpoints.

As a pioneering work, BTS [32] estimates a 3D density field from a single view, relying solely on photometric consistency constraints across multiple views during training. Subsequent studies [10, 18] adopt the same training strategy for 3D scene reconstruction but often underexploit temporal photometric and geometric constraints, resulting in inconsistent 3D occupancy predictions across adjacent frames.

Another growing trend is to unleash the potential of vision foundation models (VFMs) for comprehensive 3D scene representation. As a notable example, KYN [18] leverages a large vision-language model to enrich 3D features with semantic information. However, as illustrated in Fig. 1, challenges remain, particularly with the frequent omission of critical instances, due to the indiscriminate random ray sampling process. SC-DepthV3 [25] uses pre-

*Corresponding author: Rui Fan.

dictions from LeReS [34] as pseudo depth for robust unsupervised depth estimation. Nevertheless, current VFMs generally produce monocular depth predictions with inherent scale ambiguity [33], which are not directly applicable to temporal photometric alignment. The recently proposed VFM, Depth Anything V2 [17], demonstrates exceptional zero-shot performance in metric depth estimation with fine-grained details. However, it experiences a significant performance decline due to domain discrepancies between the training and test data.

To address the aforementioned challenges, we introduce ViPOcc, a novel approach that leverages visual priors from VFMs for fine-grained, instance-aware 3D scene reconstruction. Unlike previous state-of-the-art (SoTA) methods that solely utilize photometric discrepancies as supervisory signals, our method incorporates a depth prediction branch, which fully exploits inter-frame photometric consistency and intra-frame geometric reconstruction consistency, enabling self-supervised training with spatial-temporal consistency constraints.

Specifically, we design an inverse depth alignment module that mitigates the discrepancies between VFM predictions and depth ground truth, leading to compelling metric depth estimation results. To further enhance both the efficiency and accuracy of 3D occupancy prediction, we develop a semantic-guided, non-overlapping Gaussian mixture (SNOG) sampler, which effectively addresses issues such as redundant ray sampling and the overlooking of crucial instances prevalent in previous methods. Additionally, we propose a temporal alignment loss and a reconstruction consistency loss, which further improve the quality of both metric depth and 3D occupancy predictions. Extensive experiments on the KITTI-360 and KITTI Raw datasets validate the effectiveness of each developed component and further demonstrate ViPOcc’s superior performance over all existing SoTA methods.

In a nutshell, we present the following key contributions:

1. We propose **ViPOcc**, a single-view 3D **O**ccupancy prediction framework that incorporates **V**isual **P**riors from VFMs, achieving SoTA performance in both monocular depth estimation and 3d occupancy prediction tasks.
2. We introduce an inverse depth alignment module that effectively recovers the scale of the VFM’s depth predictions while preserving their local visual details.
3. We present a SNOG sampler that guides the framework to focus more on crucial instances and avoid overlapping patches during ray sampling.
4. We establish a novel training paradigm that couples the unsupervised training of 3D occupancy prediction and monocular depth estimation using the proposed temporal alignment and reconstruction consistency losses.

2. Related Work

2.1. Single-View 3D Occupancy Prediction

Deriving voxelized 3D occupancy of a scene from a single image is a promising technique for achieving fine-grained geometric representation and comprehensive environmental understanding in 3D space [39]. As a pioneering work, MonoScene [2] leverages voxel features generated through view projection for occupancy regression. However, this method is not suitable for real-time multi-view 3D reconstruction due to the inefficiency of voxel representations. TPVFormer [12] extends it to a multi-camera setup by incorporating tri-perspective view representations. Despite their compelling performance, these supervised methods necessitate data with 3D ground truth, which requires labor-intensive human annotation. Recently, the study [32] introduced BTS, a fully unsupervised method that uses perspective and fisheye video sequences to reconstruct driving scenes with NeRF-based volume rendering techniques. Following this work, KYN [18] leverages meaningful semantic and spatial context for fine-grained 3D scene reconstruction. MVBTS [10] combines density fields from multi-view images through knowledge distillation, achieving SoTA performance in handling occluded regions. Different from existing NeRF-based frameworks, we incorporate an additional depth prediction branch for spatial-temporal 3D occupancy alignment.

2.2. Visual Priors for 3D Scene Reconstruction

Previous studies [18, 37] have integrated visual priors from pre-trained VFMs into depth estimation and NeRF-based 3D scene reconstruction frameworks. Existing depth estimation methods typically utilize pre-inferred semantics for fine-grained feature representation and fusion [3, 9, 14]. Other studies [15, 21] leverage 2D visual priors for 3D feature representation and registration. KYN [18] incorporates a pre-trained vision-language network for robust 3D feature representation, significantly improving 3D shape recovery. MonoOcc [40] employs a pre-trained InternImage-XL [28] as its backbone for visual feature extraction and distillation. OccNeRF [37] utilizes frozen VFMs for 2D semantic supervision but faces challenges in detecting small instances due to the limitations of open-vocabulary models in capturing fine details. While these methods have successfully leveraged the strengths of VFMs for feature extraction, the informative visual priors from VFMs remain underutilized. In this paper, we leverage semantic priors from GroundedSAM [22] and spatial priors from Depth Anything V2 [17] for efficient ray sampling and spatial-temporal 3D occupancy alignment.

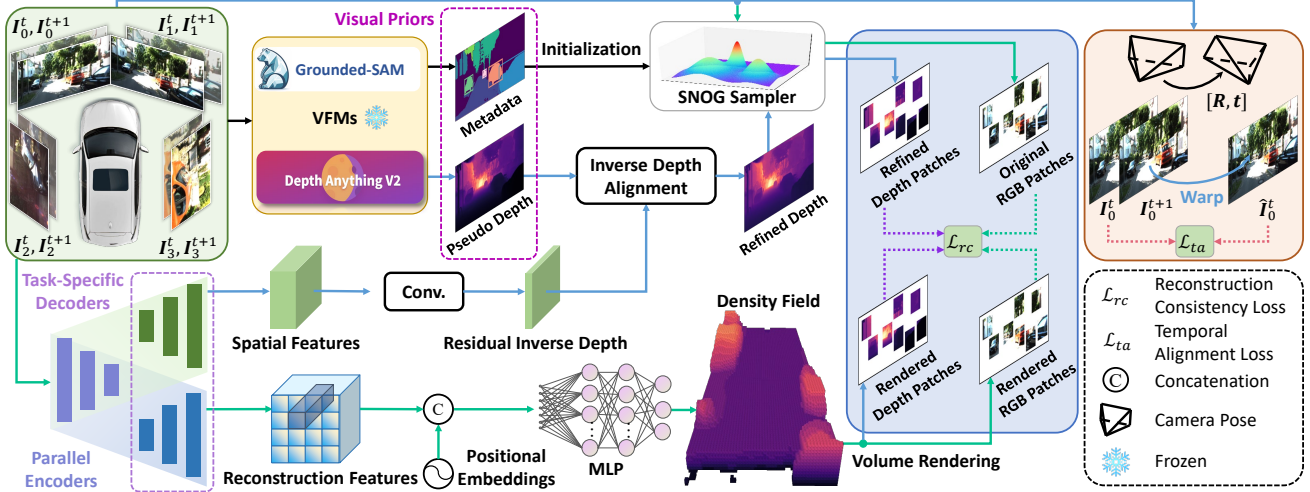


Figure 2. An illustration of our proposed **ViPOcc** framework. Unlike **previous approaches** that rely solely on NeRF for 3D scene reconstruction, ViPOcc introduces an additional **depth prediction branch** and an instance-aware SNOG sampler for **temporal photometric alignment** and **spatial geometric alignment**.

2.3. Unsupervised Monocular Depth Estimation

Existing frameworks typically maximize photometric consistency across video sequences or stereo image pairs to estimate scale-invariant depth maps. SfMLearner [41], the first reported study in this field, jointly estimates depth maps and camera poses between successive video frames by minimizing a photometric reprojection loss. Building on this method, Monodepth2 [7] introduces a minimum reprojection loss to address occlusion issues and an automasking loss to exclude moving objects that appear stationary relative to the camera. Subsequent studies mainly explored various network architectures [29, 30], dynamic object filtering strategies [26, 35], and additional constraints [9, 23]. Other NeRF-based frameworks [10, 32] estimate metric depth maps through discrete volume rendering. However, their predictions often lack accuracy and fail to preserve clear object contours. In contrast, our proposed ViPOcc utilizes visual priors from VFMs to enable instance-aware ray sampling and fine-grained metric depth estimation.

3. Methodology

3.1. Problem Setup

Given an input RGB image I and its corresponding intrinsic matrix K , we aim to reconstruct the 3D geometry of the entire scene with the voxelized density:

$$\sigma_p = \mathcal{R}(p, I, K, \Theta), \quad (1)$$

where p denotes a 3D point in the reconstructed scene, and $\mathcal{R}(\cdot)$ represents the neural radiance field with learnable parameters Θ . σ_p can be further employed to produce a rendered RGB image \hat{I}_r and a rendered distance map \hat{D}_r using

the following expressions:

$$\hat{I}_r(p_i) = \sum_{i=1}^M T_i \alpha_i c_{p_i}, \quad \hat{D}_r(p_i) = \sum_{i=1}^M T_i \alpha_i d_i, \quad (2)$$

where $\alpha_i = 1 - \exp(-\sigma_{p_i} \|\mathbf{p}_{i+1} - \mathbf{p}_i\|_2)$ denotes the probability that the ray ends between \mathbf{p}_i and \mathbf{p}_{i+1} , $T_i = \prod_{j=1}^{i-1} (1 - \alpha_j)$ represents the accumulated transmittance, c_{p_i} denotes the sampled RGB value from other viewpoints, and d_i represents the distance between \mathbf{p}_i and the ray origin.

3.2. Architecture Overview

As illustrated in Fig. 2, ViPOcc takes stereo image pairs $I_{0,1}^{t,t+1}$ and rectified fisheye images $I_{2,3}^{t,t+1}$ captured at timestamps t and $t+1$ as input. I_0^t is regarded as the principal frame, from which spatial features F_s and reconstruction features F_r are extracted using parallel encoders and task-specific decoders. During training, ViPOcc simultaneously generates 2D depth maps and 3D density fields from two separate branches. In the depth estimation branch, an inverse depth alignment module is designed to mitigate the domain discrepancy between depth priors from a VFM and the depth ground truth. The refined depth maps \hat{D} and the corresponding RGB images are then fed into our developed SNOG sampler for efficient ray sampling, producing instance-aware and non-overlapping patches. On the other hand, in the 3D occupancy prediction branch, F_r combined with positional embeddings F_p is passed through an MLP to predict a 3D density field, which is then utilized in volume rendering to generate depth and RGB patches. By enforcing reconstruction consistency across sampled RGB and depth patches, as well as temporal photometric consistency

tency between adjacent principal frames, we achieve improved performance in both 3D occupancy prediction and metric depth estimation.

3.3. Inverse Depth Alignment

Unlike prior arts [10, 32] that rely solely on NeRF-based reconstruction consistency to supervise framework training, we incorporate inter-frame photometric consistency and depth rendering consistency through a VFM-driven depth estimation branch. Pseudo depth maps D_p are first obtained from off-the-shelf VFMs like Depth Anything V2 [17]. Nevertheless, as demonstrated in our experiments, the residuals between pseudo and ground-truth depth data exhibit dramatically deviated distributions. These deviations arise from significant domain gaps between real-world scenarios and the data on which VFMs are initially trained. Therefore, it is imperative to refine depth before utilizing it to introduce additional constraints for temporal photometric alignment. As discussed in [11], neural networks often struggle to converge or maintain accuracy when fitting large ranges of numerical variations. It is thus plausible to fit residual inverse depth in our task, expressed as $\mathcal{F}(\mathbf{x}) := \frac{1}{\hat{D}(\mathbf{x})} - \frac{1}{D_p(\mathbf{x})}$, where $\mathcal{F}(\cdot)$ denotes the residual inverse depth function, \hat{D} represents the refined depth map, and \mathbf{x} denotes a given 2D pixel. This function can be effectively fitted using spatial features \mathbf{F}_s by formulating it as $\mathcal{F}(\mathbf{x}) = f(\mathbf{F}_s, \theta)$, where $f(\cdot)$ denotes a convolutional layer with learnable parameters θ . The refined depth map can therefore be yielded as follows:

$$\hat{D}(\mathbf{x}) = \frac{1}{\frac{1}{D_p(\mathbf{x})} + f(\mathbf{F}_s, \theta) + \epsilon}, \quad (3)$$

where ϵ is a small constant used to prevent the denominator from being zero. \hat{D} can then be used to ensure inter-frame photometric consistency and depth rendering consistency.

3.4. Semantic-Guided Non-Overlapping Gaussian Mixture Sampler

Focusing on individual instances rather than the entire scene can lead to more detailed and fine-grained 3D scene reconstruction. However, as shown in Fig. 3, previous SoTA approaches [18, 32] typically adopt a random patch sampler for uniform ray sampling across the entire scene, leading to redundant samples and overlooked instances. In contrast, our proposed SNOG sampler leverages informative visual priors from the pre-trained open-vocabulary model Grounded-SAM [22] (a combination of Grounding DINO [20] and SAM [16]) to optimize the allocation of computational resources while enhancing the awareness of crucial instances.

Specifically, we utilize the semantic labels from the Cityscapes dataset [4] as prompts for Grounding DINO.

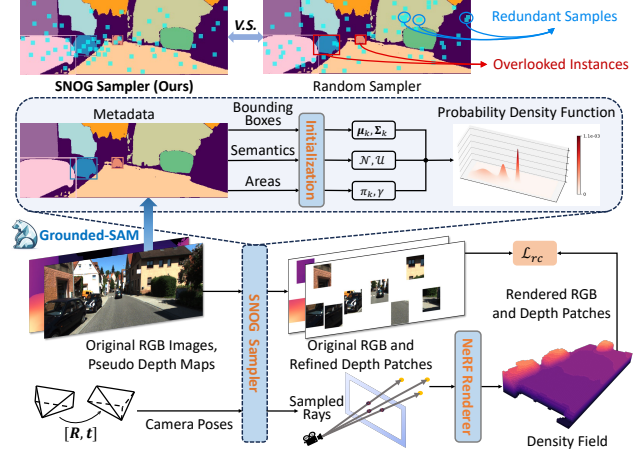


Figure 3. An illustration of our proposed SNOG sampler.

After obtaining instance-level bounding boxes, we employ SAM to generate precise segmentation masks. Consequently, for the k -th instance, we acquire its metadata $\mathcal{M}_k = \{\mathbf{l}_k, \mathbf{b}_k, s_k\}$, where \mathbf{l}_k denotes the center location of its bounding box, \mathbf{b}_k stores half of the height and width of its bounding box, and s_k indicates the semantic area of the instance. Subsequently, we use Gaussian mixture distribution combined with background uniform distribution to achieve instance-aware and non-overlapping ray sampling, the probability density function (PDF) $p(\mathbf{x})$ of which can be formulated as follows:

$$p(\mathbf{x}) = (1 - \gamma) \sum_{k=1}^K \pi_k \mathcal{N}(\mathbf{x} | \boldsymbol{\mu}_k, \boldsymbol{\Sigma}_k) + \gamma \mathcal{U}(\mathbf{x} | s), \quad (4)$$

where $\mathcal{N}(\mathbf{x} | \boldsymbol{\mu}_k, \boldsymbol{\Sigma}_k)$ denotes the PDF of the bivariate normal distribution with mean vector $\boldsymbol{\mu}_k$ and covariance matrix $\boldsymbol{\Sigma}_k$, $\mathcal{U}(\mathbf{x} | s)$ denotes the PDF of a 2D uniform distribution within the area s , and γ and π_k denote the weights of the background sampling and independent Gaussian distributions, respectively.

For the Gaussian distribution of the k -th instance, our objectives are to 1) locate $\boldsymbol{\mu}_k$ at the center of its bounding box and 2) ensure that approximately 95.5% of the samples fall within the bounding box. We can therefore initialize the parameters in (4) as follows:

$$\begin{cases} \boldsymbol{\mu}_k = \mathbf{l}_k, & \boldsymbol{\Sigma}_k = \text{diag} \left(\frac{\mathbf{b}_k \circ \mathbf{b}_k}{4} \right) \\ \pi_k = \frac{\log s_k}{\log \prod_{k=1}^K s_k} \end{cases}, \text{ for } k = 1, \dots, K, \quad (5)$$

where \circ denotes the Hardmard product operation, and π_k is normalized in logarithmic space to prevent the sampling probability of smaller instances from approaching zero, especially when the semantic areas vary significantly among instances.

Additionally, to address the redundant sampling issue, we incorporate constraints between the sampling PDF and existing samples, and formulate the final conditioned sampling PDF as follows:

$$P(\mathbf{x} | \mathcal{X}) = \begin{cases} 0, & \text{if } \exists \mathbf{x}_i \in \mathcal{X}, \|\mathbf{x} - \mathbf{x}_i\|_2^2 < 2l^2 \\ p(\mathbf{x}), & \text{otherwise} \end{cases} \quad (6)$$

where l is the patch size, and \mathcal{X} is an anchor set storing existing samples. With the final PDF, we randomly sample a collection of well-distributed and non-overlapping patches for image rendering and depth reconstruction. More details on the parameter initialization and the mathematical derivations of the PDF are given in our supplement.

3.5. Loss Formulation

A reference image can be warped to the target view using camera intrinsic parameters and differentiable grid sampling when its per-pixel depth is known. The original target image and the warped reference image should exhibit temporal photometric consistency. Furthermore, when performing volume rendering on a given frame, the rendered RGB and depth images should be respectively consistent with the original RGB image and the predicted metric depth map, thereby satisfying spatial reconstruction consistency. Therefore, we formulate a novel loss function as follows:

$$\mathcal{L} = \lambda_1 \mathcal{L}_{ta} + \lambda_2 (\mathcal{L}_{rc}^d + \mathcal{L}_{rc}^{rgb}), \quad (7)$$

where \mathcal{L}_{ta} denotes the temporal alignment loss, \mathcal{L}_{rc}^d and \mathcal{L}_{rc}^{rgb} represent the reconstruction consistency losses for depth and RGB image rendering, respectively, and λ_1 and λ_2 are the weighting parameters used to balance these two types of losses.

3.5.1. Temporal Alignment Loss

The homogeneous coordinates $\tilde{\mathbf{x}}^t$ and $\tilde{\mathbf{x}}^{t+1}$ in adjacent principal frames \mathbf{I}_0^t and \mathbf{I}_0^{t+1} are related as follows:

$$\tilde{\mathbf{x}}^{t+1} = \hat{D}^t(\mathbf{x}) \mathbf{K} \mathbf{T} \mathbf{K}^{-1} \tilde{\mathbf{x}}^t, \quad (8)$$

where \mathbf{T} denotes the relative camera pose. Therefore, we can warp \mathbf{I}_0^{t+1} into the pixel grid of \mathbf{I}_0^t using differentiable grid sampling, producing a synthesized image $\hat{\mathbf{I}}_0^t$. The temporal alignment loss, expressed as follows:

$$\mathcal{L}_{ta} = \frac{1}{N} \sum_{\mathbf{x}} M(\mathbf{x}) \left| \mathbf{I}_0^t(\mathbf{x}) - \hat{\mathbf{I}}_0^t(\mathbf{x}) \right|, \quad (9)$$

can be computed to enforce photometric similarity across adjacent frames, where M represents the weight mask detailed in [1] and N denotes the number of valid pixels for loss computation.

3.5.2. Reconstruction Consistency Loss

It is common preliminaries that $D(\mathbf{x})\tilde{\mathbf{x}} = \mathbf{K}\mathbf{p}$ and $\|\mathbf{p}\|_2 = \hat{D}_r(\mathbf{x})$. We can therefore use these relations to establish criteria for depth reconstruction consistency as follows:

$$\mathcal{L}_{rc}^d = \frac{1}{M} \sum_{\mathbf{x}} \left| \frac{\hat{D}_r(\mathbf{x})}{\|\mathbf{K}^{-1}\tilde{\mathbf{x}}\|_2} - \hat{D}(\mathbf{x}) \right|, \quad (10)$$

where M denotes the number of valid pixels for loss computation. In addition, to enforce the consistency between the original and rendered RGB patches, we adopt the same rendering loss as detailed in [32]:

$$\mathcal{L}_{rc}^{rgb} = \beta_1 \text{SSIM}(\mathbf{I}, \hat{\mathbf{I}}_r) + \beta_2 \left\| \mathbf{I} - \hat{\mathbf{I}}_r \right\|_1, \quad (11)$$

where $\beta_1 = 0.85$ and $\beta_2 = 0.15$ are the empirical parameters used in [32].

4. Experiments

4.1. Datasets, Metrics, and Implementation Details

The 3D reconstruction performance of our proposed method is evaluated on the KITTI-360 dataset [19] and the KITTI Raw dataset [6], both providing time-stamped stereo images along with ground-truth camera poses for the evaluation of scene perception algorithms. All images are resized to the resolution of 192×640 pixels, and the depth range is capped at 80m in both datasets. Following [32], we split the KITTI-360 dataset into a training set of 98,008 images, a validation set of 11,451 images, and a test set of 446 images for the 3D occupancy prediction task. We adopt the Eigen split [7] for depth estimation on the KITTI Raw dataset. Moreover, we use the DDAD dataset [8] to evaluate our model’s zero-shot generalizability using the weights obtained on the KITTI-360 dataset. The input images, with the original resolution of $1,216 \times 1,936$ pixels, are center-cropped and resized to 192×640 pixels for fair comparison.

Following the experimental protocols established in previous works [18, 32], we quantify the 3D occupancy prediction performance of the model using the following metrics: scene occupancy accuracy O_{acc}^s , invisible scene accuracy IE_{acc}^s , invisible scene recall IE_{rec}^s , object occupancy accuracy O_{acc}^o , invisible object accuracy IE_{acc}^o , and invisible object recall IE_{rec}^o . Furthermore, we use the mean absolute relative error (Abs Rel), mean squared relative error (Sq Rel), root mean squared error (RMSE), root mean squared log error (RMSE log), and accuracy under certain thresholds ($\delta_i < 1.25^i, i = 1, 2, 3$) to quantify the model’s monocular depth estimation performance.

The proposed method is trained on an NVIDIA RTX 4090 GPU using the Adam optimizer for 25 epochs, with an initial learning rate of $1e-4$, which is reduced by a factor of 10 during the final 10 epochs. We use BTS [32] as

Method	$O_{acc}^s \uparrow$	$IE_{acc}^s \uparrow$	$IE_{rec}^s \uparrow$
Monodepth2 [7]	0.90	N/A	N/A
Monodepth2 + 4m	0.90	0.59	0.66
PixelNeRF [36]	0.89	0.62	0.60
BTS [32]	0.92	0.69	0.64
KYN [18]	0.92	0.70	0.66
ViPOcc (Ours)	0.93	0.71	0.69

Table 1. Comparison of scene reconstruction performance on the KITTI-360 dataset.

Method	$O_{acc}^o \uparrow$	$IE_{acc}^o \uparrow$	$IE_{rec}^o \uparrow$
Monodepth2 [7]	0.69	N/A	N/A
Monodepth2 + 4m	0.70	0.53	0.52
PixelNeRF [36]	0.67	0.53	0.49
BTS [32]	0.79	0.69	0.60
KYN [18]	0.79	0.69	0.61
ViPOcc (Ours)	0.79	0.69	0.64

Table 2. Comparison of object reconstruction performance on the KITTI-360 dataset.

our baseline network and adopt the metric depth predictions from Depth Anything V2 [33] as pseudo depth. We use Grounded-SAM [22] to generate instance-level semantic masks and bounding boxes.

4.2. Comparisons with State-of-The-Art Methods

4.2.1. 3D Occupancy Prediction

Following the experimental protocols detailed in the study [32], we compare ViPOcc with a representative self-supervised monocular depth estimation network Monodepth2 [7] and other NeRF-based SoTA methods in terms of 3D occupancy prediction performance, as presented in Tables 1 and 2. Specifically, when evaluating Monodepth2’s 3D occupancy prediction performance, all points behind visible pixels in the image are considered occupied. This is primarily due to the infeasibility of inferring the true 3D geometry of points that are invisible in the image. Furthermore, we also follow prior studies [18, 32] to quantify the model’s performance by considering points within a distance of up to 4m from visible points as occupied.

It can be observed that ViPOcc achieves SoTA performance across all metrics in 3D occupancy prediction for both scene and object reconstruction. Notably, O_{acc}^s , O_{rec}^s , and O_{rec}^o increase by 1.1-3.4%, 4.6-15.0%, and 4.9-30.6%, respectively. It is also worth noting that Monodepth2 + 4m can deliver competitive performance in O_{acc}^s and O_{acc}^o .

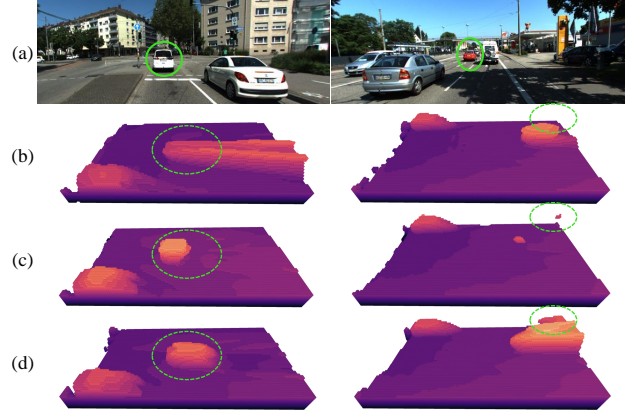


Figure 4. Qualitative comparison of 3D occupancy prediction on the KITTI-360 dataset: (a) input RGB images; (b) BTS results; (c) KYN results; (d) our results. A darker voxel color indicates a lower altitude.

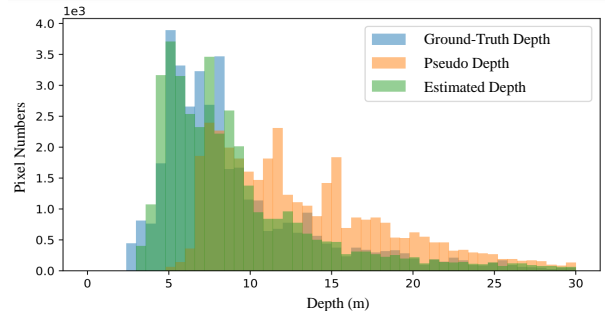


Figure 5. Depth distribution comparison.

However, it relies on hand-crafted criteria rather than directly learning the 3D structure from a single view [18].

Qualitative comparisons are presented in Fig. 4, where the predicted occupancy grids are viewed from the right side of the scene. It is evident that our method significantly outperforms both BTS and KYN in 3D geometry reconstruction, particularly for crucial instances, and effectively reduces trailing effects. These results demonstrate the efficacy of ViPOcc in reasoning about occluded regions against inherent ambiguities.

4.2.2. Metric Depth Estimation

Table 4 shows the comparison of metric depth estimation performance among VFM, previous SoTA methods, and our proposed ViPOcc on the KITTI-360 dataset. It is evident that the depth predictions from Depth Anything V2 [17] are unsatisfactory, regardless of whether median scaling is used to align the depth distribution. Notably, ViPOcc demonstrates superior performance compared to existing NeRF-based unsupervised methods, achieving a decrease of 5.8% in Abs Rel. Moreover, we compare depth distri-

Method	Abs Rel ↓	Sq Rel ↓	RMSE ↓	RMSE log ↓	$\delta < 1.25 \uparrow$	$\delta < 1.25^2 \uparrow$	$\delta < 1.25^3 \uparrow$
Monodepth2 [7]	0.106	0.818	4.750	0.196	0.874	0.957	0.979
SwinDepth [24]	0.106	0.739	4.510	0.182	0.890	0.964	0.984
Lite-Mono [38]	0.107	0.765	4.561	0.183	0.886	0.963	0.983
Dynamo-Depth [26]	0.112	0.758	4.505	0.183	0.873	0.959	0.984
BTS [32]	0.102	0.755	4.409	0.188	0.882	0.961	0.982
MVBTS [10]	0.105	0.757	4.501	0.193	0.873	0.957	0.981
KDBTS [10]	0.105	0.761	4.498	0.193	0.873	0.957	0.981
ViPOcc (Ours)	0.096	0.652	4.507	0.179	0.890	0.964	0.983

Table 3. Comparison of depth estimation performance on the KITTI Raw dataset using the Eigen split.

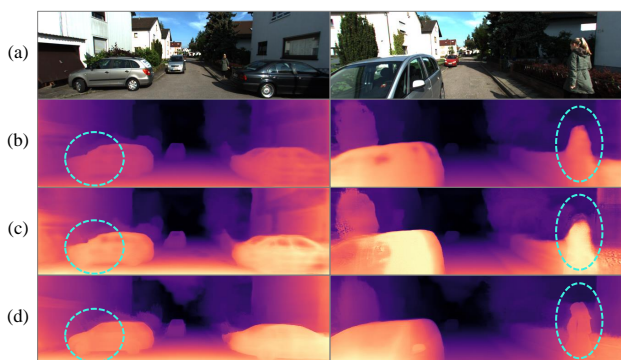


Figure 6. Comparison of metric depth estimation on the KITTI-360 dataset: (a) input RGB images; (b) BTS results; (c) KYN results; (d) our results.

Method	Abs Rel	RMSE log	$\alpha < 1.25$
Pseudo depth (no scaling)	0.586	0.477	0.071
Pseudo depth (median scaling)	0.142	0.209	0.832
BTS [32]	0.103	0.194	0.891
KYN [18]	0.107	0.197	0.880
ViPOcc (Ours)	0.097	0.188	0.886

Table 4. Comparison of metric depth estimation performance on the KITTI-360 dataset.

butions among ground-truth depth, pseudo depth, and our predictions. As illustrated in Fig. 5, significant discrepancies among these distributions not only underscore the infeasibility of directly using pseudo depth to generate supervisory signals, but also validate the effectiveness of our proposed inverse depth alignment module in refining depth.

As presented in Fig. 6, the qualitative comparison with prior SoTA methods on the KITTI-360 dataset demonstrates ViPOcc’s exceptional metric depth estimation performance. Our method exhibits superior depth consistency in continu-

ous regions, as shown on the vehicle’s glass, and preserves clear object boundaries, as shown on the pedestrian. These improvements can be attributed to the spatial reconstruction consistency constraint we incorporated between rendered and predicted depth maps, which also preserves the local differential properties of VFM predictions to enable fine-grained depth estimation.

Moreover, as presented in Table 3, ViPOcc also demonstrates superior depth estimation performance compared to all existing self-supervised methods on the KITTI Raw dataset. Specifically, it achieves a decrease of 5.9% in Abs Rel and 11.8% in Sq Rel compared to previous SoTA approaches. Surprisingly, ViPOcc significantly outperforms its counterparts trained with the same NeRF-based architectures, such as BTS [32], MVBTS [10], and KDBTS [10]. It achieves an average error reduction of 9.5% in Abs Rel and an average performance gain of 1.3% in δ_1 . These experimental results underscore the effectiveness of our proposed ViPOcc framework for monocular depth estimation across different scenarios with distinct experimental setups.

4.3. Ablation Studies

We validate the rationality and efficacy of ViPOcc through extensive ablation studies, specifically focusing on depth estimation methods, ray sampling strategies, and loss function designs, as presented in Table 5.

We first adopt an individual depth prediction branch without VFM’s visual priors incorporated for depth estimation, resulting in performance similar to that of the baseline. We attribute this phenomenon to a performance bottleneck within the depth prediction network, due to its estimations not being sufficiently accurate, which in turn limits improvements in 3D occupancy prediction. We then investigate the effectiveness of aligning VFM’s depth priors based on depth residuals. As discussed earlier, neural networks struggle to converge or maintain accuracy when fitting depth residuals, which typically exhibit a large range of numerical variations. Consequently, a drastic performance

Configuration		$O_{acc}^s \uparrow$	$IE_{acc}^s \uparrow$	$IE_{rec}^s \uparrow$
Baseline [32]		0.91	0.65	0.64
Depth estimation	+ Depth	0.91	0.64	0.64
	+ Pseudo depth	0.86	0.60	0.61
	+ Inverse pseudo depth	0.92	0.65	0.66
Ray sampling	+ Random sampler	0.91	0.65	0.64
	+ SNOG sampler	0.92	0.67	0.67
Loss	+ \mathcal{L}_{ta}	0.91	0.66	0.64
	+ \mathcal{L}_{rc}	0.89	0.64	0.60
	+ $\mathcal{L}_{ta}, \mathcal{L}_{rc}$	0.92	0.69	0.67
Full implementation		0.93	0.71	0.69

Table 5. Ablation studies of ViPOcc inner designs on the KITTI-360 dataset.

Method	Abs Rel	RMSE log	$\alpha < 1.25$
BTS [32]	0.182	0.290	0.746
KYN [18]	0.190	0.286	0.749
ViPOcc (Ours)	0.175	0.282	0.749

Table 6. Zero-shot depth estimation performance comparison on the DDAD dataset.

drop occurs, falling within our expectations. When employing our proposed inverse depth alignment module, a notable performance improvement in 3D occupancy prediction is achieved, demonstrating its effectiveness.

Moreover, as observed, the SNOG sampler leads to improved performance, particularly in invisible scene accuracy and recall, which increase by 3.1-4.7%. This validates the effectiveness of our proposed ray sampling strategy. Additional comparisons between random and SNOG samplers regarding their efficiency are provided in our supplement.

In addition, it is evident that relying solely on temporal alignment loss yields limited performance improvements, whereas using only the reconstruction consistency loss actually degrades the framework’s performance. However, combining both losses significantly enhances 3D occupancy prediction performance, leading to an increase of approximately 4.7-6.2% in invisible scene accuracy and recall.

4.4. Zero-Shot Depth Estimation

To further evaluate the generalizability of ViPOcc, we conduct a zero-shot test on the DDAD dataset [8] using the pre-trained weights obtained from the KITTI-360 dataset. As presented in Table 6, ViPOcc outperforms other SoTA methods in zero-shot depth estimation, demonstrating its exceptional generalizability.

5. Conclusion

This paper introduced ViPOcc, a novel framework that effectively leverages VFM’s visual priors for single-view 3D occupancy prediction. ViPOcc consists of two coupled branches: one estimates highly accurate metric depth by aligning the inverse depth output from Depth Anything V2, while the other one predicts 3D occupancy with a Grounded-SAM-guided Gaussian mixture sampler incorporated to achieve efficient and instance-aware ray sampling. These two branches are effectively coupled through a temporal photometric alignment loss and a spatial geometric consistency loss. Extensive experiments and comprehensive analyses validate the effectiveness of our novel contributions and the superior performance of ViPOcc compared to previous SoTA methods. In the future, we aim to achieve a tighter coupling of these two branches and develop a more lightweight 3D occupancy prediction framework.

References

- [1] Jiawang Bian et al. Unsupervised Scale-Consistent Depth and Ego-Motion Learning from Monocular Video. *Advances in Neural Information Processing Systems (NeurIPS)*, 32, 2019. 5
- [2] Anh-Quan Cao and Raoul De Charette. MonoScene: Monocular 3D Semantic Scene Completion. In *Proceedings of the IEEE/CVF Conference on Computer Vision and Pattern Recognition (CVPR)*, pages 3991–4001, 2022. 1, 2
- [3] Xingyu Chen et al. Self-Supervised Monocular Depth Estimation: Solving the Edge-Fattening Problem. In *Proceedings of the IEEE/CVF Winter Conference on Applications of Computer Vision (WACV)*, pages 5776–5786, 2023. 2
- [4] Marius Cordts et al. The Cityscapes Dataset for Semantic Urban Scene Understanding. In *Proceedings of the IEEE/CVF Conference on Computer Vision and Pattern Recognition (CVPR)*, pages 3213–3223, 2016. 4, 11
- [5] Jia Deng et al. ImageNet: A large-scale hierarchical image database. In *Proceedings of the IEEE/CVF Conference on Computer Vision and Pattern Recognition (CVPR)*, pages 248–255. IEEE, 2009. 11
- [6] Andreas Geiger et al. Vision Meets Robotics: the KITTI Dataset. *The International Journal of Robotics Research*, 32(11):1231–1237, 2013. 5, 13
- [7] Clément Godard et al. Digging into Self-Supervised Monocular Depth Estimation. In *Proceedings of the IEEE/CVF International Conference on Computer Vision (ICCV)*, pages 3828–3838, 2019. 3, 5, 6, 7, 11, 13
- [8] Guizilini et al. 3D Packing for Self-Supervised Monocular Depth Estimation. In *Proceedings of the IEEE/CVF Conference on Computer Vision and Pattern Recognition (CVPR)*, pages 2485–2494, 2020. 5, 8, 13
- [9] Vitor Guizilini et al. Semantically-Guided Representation Learning for Self-Supervised Monocular Depth. *arXiv preprint arXiv:2002.12319*, 2020. 2, 3
- [10] Keonhee Han et al. Boosting Self-Supervision for Single-View Scene Completion via Knowledge Distillation. In *Pro-*

- ceedings of the *IEEE/CVF Conference on Computer Vision and Pattern Recognition (CVPR)*, pages 9837–9847, 2024. [1](#), [2](#), [3](#), [4](#), [7](#)
- [11] Kaiming He et al. Deep Residual Learning for Image Recognition. In *Proceedings of the IEEE/CVF Conference on Computer Vision and Pattern Recognition (CVPR)*, pages 770–778, 2016. [4](#), [11](#)
- [12] Yuanhui Huang et al. Tri-Perspective View for Vision-Based 3D Semantic Occupancy Prediction. In *Proceedings of the IEEE/CVF Conference on Computer Vision and Pattern Recognition (CVPR)*, pages 9223–9232, 2023. [1](#), [2](#)
- [13] Yuanhui Huang et al. SelfOcc: Self-Supervised Vision-Based 3D Occupancy Prediction. In *Proceedings of the IEEE/CVF Conference on Computer Vision and Pattern Recognition (CVPR)*, pages 19946–19956, 2024. [1](#)
- [14] Hyunyoung Jung et al. Fine-Grained Semantics-Aware Representation Enhancement for Self-Supervised Monocular Depth Estimation. In *Proceedings of the IEEE/CVF International Conference on Computer Vision (ICCV)*, pages 12642–12652, 2021. [2](#)
- [15] Justin Kerr et al. LERF: Language Embedded Radiance Fields. In *Proceedings of the IEEE/CVF International Conference on Computer Vision (ICCV)*, pages 19729–19739, 2023. [2](#)
- [16] Alexander Kirillov et al. Segment Anything. In *Proceedings of the IEEE/CVF International Conference on Computer Vision (ICCV)*, pages 4015–4026, 2023. [4](#), [11](#)
- [17] L. Yang et al. Depth Anything V2. *arXiv preprint arXiv:2406.09414*, 2024. [2](#), [4](#), [6](#), [12](#)
- [18] Rui Li et al. Know Your Neighbors: Improving Single-View Reconstruction via Spatial Vision-Language Reasoning. In *Proceedings of the IEEE/CVF Conference on Computer Vision and Pattern Recognition (CVPR)*, pages 9848–9858, 2024. [1](#), [2](#), [4](#), [5](#), [6](#), [7](#), [8](#), [11](#), [12](#), [13](#), [14](#), [15](#), [16](#)
- [19] Yiyi Liao et al. KITTI-360: A Novel Dataset and Benchmarks for Urban Scene Understanding in 2D and 3D. *IEEE Transactions on Pattern Analysis and Machine Intelligence*, 45(3):3292–3310, 2022. [5](#), [12](#), [15](#), [16](#)
- [20] Shilong Liu et al. Grounding DINO: Marrying DINO with Grounded Pre-Training for Open-Set Object Detection. In *European Conference on Computer Vision*, pages 38–55. Springer, 2025. [4](#), [11](#)
- [21] Songyou Peng et al. OpenScene: 3D Scene Understanding with Open Vocabularies. In *Proceedings of the IEEE/CVF Conference on Computer Vision and Pattern Recognition (CVPR)*, pages 815–824, 2023. [2](#)
- [22] Tianhe Ren et al. Grounded SAM: Assembling Open-World Models for Diverse Visual Tasks. *arXiv preprint arXiv:2401.14159*, 2024. [2](#), [4](#), [6](#), [12](#)
- [23] Aron Schmied et al. R3D3: Dense 3D Reconstruction of Dynamic Scenes from Multiple Cameras. In *Proceedings of the IEEE/CVF International Conference on Computer Vision (ICCV)*, pages 3216–3226, 2023. [3](#)
- [24] Dongseok Shim and H Jin Kim. SwinDepth: Unsupervised Depth Estimation Using Monocular Sequences via Swin Transformer and Densely Cascaded Network. In *International Conference on Robotics and Automation (ICRA)*, pages 4983–4990. IEEE, 2023. [7](#)
- [25] Libo Sun et al. SC-DepthV3: Robust Self-Supervised Monocular Depth Estimation for Dynamic Scenes. *IEEE Transactions on Pattern Analysis and Machine Intelligence*, 46(1):497–508, 2024. [1](#)
- [26] Yihong Sun and Bharath Hariharan. Dynamo-Depth: Fixing Unsupervised Depth Estimation for Dynamical Scenes. *Advances in Neural Information Processing Systems (NeurIPS)*, 36, 2024. [3](#), [7](#)
- [27] Xiaoyu Tian et al. Occ3D: A large-scale 3d occupancy prediction benchmark for autonomous driving. *Advances in Neural Information Processing Systems (NeurIPS)*, 36, 2024. [1](#)
- [28] Wenhai Wang et al. InternImage: Exploring Large-Scale Vision Foundation Models with Deformable Convolutions. In *Proceedings of the IEEE/CVF Conference on Computer Vision and Pattern Recognition (CVPR)*, pages 14408–14419, 2023. [2](#)
- [29] Youhong Wang et al. SQLdepth: Generalizable Self-Supervised Fine-Structured Monocular Depth Estimation. In *Proceedings of the AAAI Conference on Artificial Intelligence (AAAI)*, pages 5713–5721, 2024. [3](#)
- [30] Jamie Watson et al. The Temporal Opportunist: Self-Supervised Multi-Frame Monocular Depth. In *Proceedings of the IEEE/CVF Conference on Computer Vision and Pattern Recognition (CVPR)*, pages 1164–1174, 2021. [3](#)
- [31] Yi Wei et al. SurroundOcc: Multi-Camera 3D Occupancy Prediction for Autonomous Driving. In *Proceedings of the IEEE/CVF International Conference on Computer Vision (ICCV)*, pages 21729–21740, 2023. [1](#)
- [32] Felix Wimbauer et al. Behind the Scenes: Density Fields for Single View Reconstruction. In *Proceedings of the IEEE/CVF Conference on Computer Vision and Pattern Recognition (CVPR)*, pages 9076–9086, 2023. [1](#), [2](#), [3](#), [4](#), [5](#), [6](#), [7](#), [8](#), [11](#), [12](#), [13](#), [14](#), [15](#), [16](#)
- [33] Lihe Yang et al. Depth Anything: Unleashing the Power of Large-Scale Unlabeled Data. In *Proceedings of the IEEE/CVF Conference on Computer Vision and Pattern Recognition (CVPR)*, pages 10371–10381, 2024. [2](#), [6](#)
- [34] Wei Yin et al. Learning to Recover 3D Scene Shape from a Single Image. In *Proceedings of the IEEE/CVF Conference on Computer Vision and Pattern Recognition (CVPR)*, pages 204–213, 2021. [2](#)
- [35] Zhichao Yin and Jianping Shi. GeoNet: Unsupervised Learning of Dense Depth, Optical Flow and Camera Pose. In *Proceedings of the IEEE/CVF Conference on Computer Vision and Pattern Recognition (CVPR)*, pages 1983–1992, 2018. [3](#)
- [36] Alex Yu et al. PixelNeRF: Neural Radiance Fields from One or Few Images. In *Proceedings of the IEEE/CVF Conference on Computer Vision and Pattern Recognition (CVPR)*, pages 4578–4587, 2021. [6](#)
- [37] Chubin Zhang et al. OccNeRF: Self-Supervised Multi-Camera Occupancy Prediction with Neural Radiance Fields. *arXiv preprint arXiv:2312.09243*, 2023. [2](#)
- [38] Ning Zhang et al. Lite-Mono: a Lightweight CNN and Transformer Architecture for Self-Supervised Monocular Depth Estimation. In *Proceedings of the IEEE/CVF Confer-*

- ence on Computer Vision and Pattern Recognition (CVPR)*, pages 18537–18546, 2023. [7](#)
- [39] Yanan Zhang et al. Vision-Based 3D Occupancy Prediction in Autonomous Driving: A Review and Outlook. *arXiv preprint arXiv:2405.02595*, 2024. [2](#)
- [40] Yupeng Zheng et al. MonoOcc: Digging into Monocular Semantic Occupancy Prediction. In *2024 IEEE International Conference on Robotics and Automation (ICRA)*, pages 18398–18405, 2024. [2](#)
- [41] Tinghui Zhou et al. Unsupervised Learning of Depth and Ego-Motion from Video. In *Proceedings of the IEEE/CVF Conference on Computer Vision and Pattern Recognition (CVPR)*, pages 1851–1858, 2017. [3](#)

A. Additional Methodological Details

A.1. Framework Architecture

For the parallel encoders, we utilize two ResNet-50 [11] backbones, each pre-trained on the ImageNet dataset [5]. These backbones share the same architecture and initialization process but differ in their self-supervisory signals. For the task-specific decoders, we adopt the architecture of Monodepth2 [7] with modifications to the final layers. As detailed in Table 7, the output features from both decoders, F_r and F_s , are upsampled to a resolution of 192×640 pixels. These features are then utilized for residual inverse depth estimation and dense 3D scene reconstruction.

A.2. SNOG Sampler

This subsection presents preliminaries on the Gaussian distribution and implementation details of the proposed SNOG sampler.

A.2.1. Gaussian Distribution

In probability theory, the normal or Gaussian distribution is a type of continuous probability distribution characterized by the following probability density function (PDF):

$$f(x) = \frac{1}{\sqrt{2\pi\sigma^2}} e^{-\frac{(x-\mu)^2}{2\sigma^2}}, \quad (\text{A.1})$$

where μ denotes the mean or expectation of the distribution, and σ represents the variance. The associated error function $\text{erf}(x)$ calculates the probability that a random variable with a normal distribution, having a mean of 0 and a variance of $\frac{1}{2}$, falls within the range $[-x, x]$, expressed as follows:

$$\text{erf}(x) = \frac{1}{\sqrt{\pi}} \int_{-x}^x e^{-t^2} dt = \frac{2}{\sqrt{\pi}} \int_0^x e^{-t^2} dt. \quad (\text{A.2})$$

Moreover, the probability that a random variable with a Gaussian distribution lies between $\mu - n\sigma$ and $\mu + n\sigma$ is given by $\text{erf}(\frac{n}{\sqrt{2}})$. Therefore, for an arbitrary normal distribution, values within two standard deviations from the mean approximately account for 95.45% of the distribution.

A.2.2. Derivation of the Sampling PDF

Specifically, we utilize processed ground-truth labels from the Cityscapes semantic segmentation task [4] as prompts for Grounding DINO [20]. As shown in Table 8, to avoid excessively detected bounding boxes and fragmented segmentation results, we exclude uncommon phrases, such as “bridge” and “tunnel”, and merge semantically similar phrases, such as “truck”, “bus”, and “caravan” provided in the original Cityscapes dataset. Furthermore, these phrases are categorized for different sampling strategies based on their physical properties. For phrases typically associated with large areas, such as “sky”, “road”, “vegetation”, and “building”, we employ a 2D uniform sampling strategy to

Task-Specific Decoders				
Layer	KS	Channels	Resolution	Activation
Conv2d	3	512→256	(6 × 20)	ELU
UpFusion	3	256	(12 × 40)	ELU
Conv2d	3	128	(12 × 40)	ELU
UpFusion	3	128	(24 × 80)	ELU
Conv2d	3	64	(24 × 80)	ELU
UpFusion	3	64	(48 × 160)	ELU
Conv2d	3	32	(48 × 160)	ELU
UpFusion	3	32	(96 × 320)	ELU
Conv2d	3	16	(96 × 320)	ELU
UpFusion	3	16	(192 × 640)	ELU
Conv2d → F_r	3	64	(192 × 640)	-
Conv2d → F_s	1	64	(192 × 640)	-

Table 7. Network architecture of task-specific decoders. “KS” represents the kernel size, and the “UpFusion” layer represents a combination of an upsampling layer, a skip connection layer, and a convolutional layer.

ensure evenly allocated attention within these areas. For critical regions, such as “car” and “pedestrian”, we adopt a Gaussian mixture sampling strategy to allow for a higher density of sampling points, thereby enhancing fine-grained 3D reconstruction performance. Moreover, we employ a uniform sampling strategy for background regions, namely “unlabeled”. Therefore, if Grounding DINO detects no objects in an input image, our SNOG sampler automatically defaults to the random uniform sampler used in previous state-of-the-art methods [18, 32].

As described in the main paper, we utilize SAM [16] to obtain the metadata $\mathcal{M}_k = \{\mathbf{l}_k, \mathbf{b}_k, s_k\}$ for the k -th instance. Therefore, the instance-level PDF $p_k(\mathbf{x}) : \mathbb{R}^{H \times W} \rightarrow [0, 1)$ can be formulated as follows:

$$p_k(\mathbf{x}) = \begin{cases} \mathcal{N}(\mathbf{x} | \boldsymbol{\mu}_k, \boldsymbol{\Sigma}_k), & \text{if } \mathcal{M}_k \in \mathcal{G} \\ \mathcal{U}(\mathbf{x} | s_k), & \text{otherwise} \end{cases} \quad (\text{A.3})$$

where \mathcal{G} denotes the Gaussian sampling metadata set. Furthermore, to derive a plausible sampling PDF for the entire scene, we employ a mixture sampling model to combine all instance-level PDFs, yielding the scene-level PDF $p(\mathbf{x})$ as

Prompt	Sampling strategy
Road	\mathcal{U}
Building	\mathcal{U}
Vegetation	\mathcal{U}
Sky	\mathcal{U}
Car	\mathcal{N}
Pedestrian	\mathcal{N}
Unlabeled	\mathcal{U}

Table 8. Grounding DINO prompts and their corresponding sampling strategies. \mathcal{N} denotes the Gaussian sampling strategy, and \mathcal{U} denotes the uniform sampling strategy.

follows:

$$\begin{aligned}
p(\mathbf{x}) &= \sum_{i=1}^N p_k(\mathbf{x}) \\
&= \sum_{k=1}^K \pi_k \mathcal{N}(\mathbf{x} \mid \boldsymbol{\mu}_k, \boldsymbol{\Sigma}_k) + \sum_{j=K+1}^N \pi_j \mathcal{U}(\mathbf{x} \mid s_k) \\
&= (1 - \gamma) \sum_{k=1}^K \pi_k \mathcal{N}(\mathbf{x} \mid \boldsymbol{\mu}_k, \boldsymbol{\Sigma}_k) + \gamma \mathcal{U}(\mathbf{x} \mid s),
\end{aligned} \tag{A.4}$$

where γ denotes the background sampling ratio, N and K denote the total number of instances and the number of Gaussian sampling instances, respectively, and $s = \sum s_k$ represents the total area of uniformly sampled regions. Based on (A.4) in the supplement, we further formulate the conditioned sampling PDF $P(\mathbf{x} \mid \mathcal{X})$ (discussed in the main paper) for efficient and instance-aware ray sampling. Qualitative visualizations of our SNOG sampler are presented in Fig. 8 in the supplement.

B. Technical Details

B.1. Implementation Details

Our implementation is based on the official code repository published by [32]. Additionally, we are inspired by the repository from [18] regarding the evaluation of 3D occupancy prediction and visualization of density fields.

B.1.1. Acquisition of Visual Priors

In practice, visual priors from VFMs are pre-generated to improve training efficiency. Specifically, within the depth prediction branch, we employ a Depth Anything V2 [17] to produce metric pseudo depth maps, which are stored as 32-bit float ndarrays. In the SNOG sampler, we use a Grounded-SAM [22] to pre-generate instance-level bounding boxes, semantic masks, and areas, as well as to compute the 2D coordinates of sampling anchors in advance. Both

the pseudo depth maps and sampling anchors are directly loaded to accelerate the training process.

B.1.2. Evaluation Protocols

During the evaluation of 3D occupancy prediction, samples are evenly distributed within a cuboid space $\mathbb{R}^{h \times w \times d}$ relative to the camera, with dimensions $w = [-4, 4]\text{m}$, $h = [-1, 0]\text{m}$, and $d = [4, 20]\text{m}$. For each voxel \mathbf{p} , the predicted density $\sigma_{\mathbf{p}}$ is discretized into a binary occupancy score $o_{\mathbf{p}} \in \{0, 1\}$ with a threshold $\tau = 0.5$.

During the evaluation of metric depth estimation, our method can produce an estimated depth map through either the depth estimation branch or the 3D occupancy prediction branch. Although their metrics are numerically close, due to the use of the reconstruction consistency loss (detailed in equation (10) in the main paper), repeated experiments have shown that the metrics of the rendered depth \hat{D}_r are often slightly superior to those of the predicted depth \hat{D} . However, \hat{D} provides much better visual quality compared to \hat{D}_r . This discrepancy can be attributed to the following two reasons:

- The 3D occupancy prediction branch employs NeRF-based volume rendering for metric depth recovery, which provides superior global structure modeling capabilities compared to methods that directly estimate depth from 2D images.
- Our proposed inverse depth alignment module effectively eliminates domain discrepancies while preserving the sharpness and detail of the original depth priors from the VFM.

Therefore, we use \hat{D}_r for evaluation and \hat{D} for visualization in all experiments.

B.2. Dataset Configuration

B.2.1. KITTI-360

As illustrated in Fig. 7, the KITTI-360 dataset [19] provides sequential frames using two stereo cameras and two fisheye cameras. Following [32], the fisheye images are resampled using a virtual perspective camera, which shares the same intrinsic parameters as the perspective forward-facing cameras. To maximize the overlap of the viewing frustums with the forward-facing cameras, we tilt the virtual camera downward by 15° . However, the fisheye and forward-facing cameras from the same timestamp typically do not overlap in their visible areas. Therefore, to enhance rendering quality, we offset the fisheye cameras by 10 timestamps, optimizing the overlap of their frustums.

Following [18], we accumulate 3D LiDAR sweeps over a period of 300 timestamps to accurately “carve out” the 3D scene geometry. Points that remain invisible in all LiDAR sweeps are considered occupied, while those visible in any sweep are considered as unoccupied.

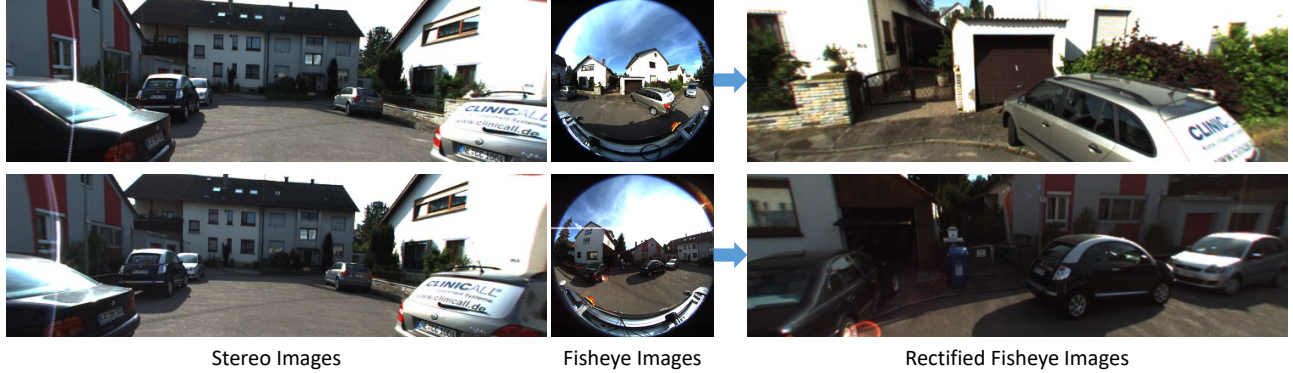


Figure 7. An illustration of stereo and fisheye images from the KITTI-360 dataset. The fisheye images are resampled using a virtual perspective camera, which shares the same intrinsic parameters as the perspective forward-facing cameras.

B.2.2. KITTI Raw

We train ViPOcc for 50 epochs on the KITTI Raw dataset [6] using the Eigen split [7]. The stereo image pairs with adjacent timestamps are fed into the network for image rendering and photometric reconstruction. Due to the absence of 3D ground-truth labels, we only report the depth estimation metrics on the KITTI Raw dataset.

B.2.3. DDAD

We evaluate the generalizability of our model using the official test set of the DDAD dataset [8]. To perform zero-shot evaluation, we directly utilize the official weights for the KITTI-360 dataset provided by BTS [32] and KYN [18]. Due to the resolution discrepancy between the KITTI-360 dataset (192×640 pixels) and the DDAD dataset ($1,216 \times 1,936$ pixels), we apply a vertical crop to align the fields of view. Additionally, to minimize differences in depth scale, we employ median scaling, adjusting the predicted depths using the ratio of median ground-truth depth to median predicted depth.

C. Additional Experimental Results

We conduct additional experiments to compare network inference speed and training parameters, evaluate the computational efficiency of ray samplers, compare the performance of 3D occupancy prediction and metric depth estimation, and select hyper-parameters for loss functions.

C.1. Network Parameters and Inference Speed

We provide network parameters and inference speed comparisons between prior works and ViPOcc. As shown in Table 9, KYN [18] has much more training parameters due to the inclusion of a large language model, while our method maintains comparable parameters to BTS [32]. The 3D occupancy and depth inference speed are tested on an NVIDIA RTX 4090D GPU using the KITTI-360 test set

Method	TP (M)	IS _o (FPS)	IS _d (FPS)
BTS [32]	43.92	81.98	10.72
KYN [18]	530.49	19.36	1.03
ViPOcc (Ours)	58.76	81.68	124.58

Table 9. Comparison of network parameters and inference speed among ViPOcc and previous SoTA methods. TP denotes Training Parameters, IS_o denotes the inference speed of 3D occupancy prediction, and IS_d denotes the inference speed of depth estimation.

containing 446 images. RGB images are resized to a resolution of 192×640 pixels before inference. ViPOcc achieves comparable 3D occupancy inference speed to BTS, while providing significantly faster depth inference compared to the other two methods. This improvement is due to our efficient depth estimation branch, which avoids the volume rendering process during depth estimation.

C.2. Ray Sampler Efficiency

Following previous studies [18, 32], we generate a total of 64 patches in each iteration, with each patch measuring 8×8 pixels. The previous random sampler often results in overlapped samples due to the absence of necessary constraints, leading to redundant computations for the same rays. This redundancy is considered unnecessary in our experiments. To evaluate the efficiency of our proposed SNOG sampler, we define N_v as the average number of valid rays sampled per iteration, and N_{vc} as the average number of valid rays sampled at crucial instances per iteration, which can be formulated as follows:

$$N_v = \frac{1}{T} \sum_{j=1}^{j=T} |\{\mathbf{r}_{i,j}\}|, \quad N_{vc} = \frac{1}{T} \sum_{j=1}^{j=T} |\{\mathbf{r}_{i,j} | \mathbf{r}_{i,j} \in \mathcal{S}_j\}|, \quad (\text{A.5})$$

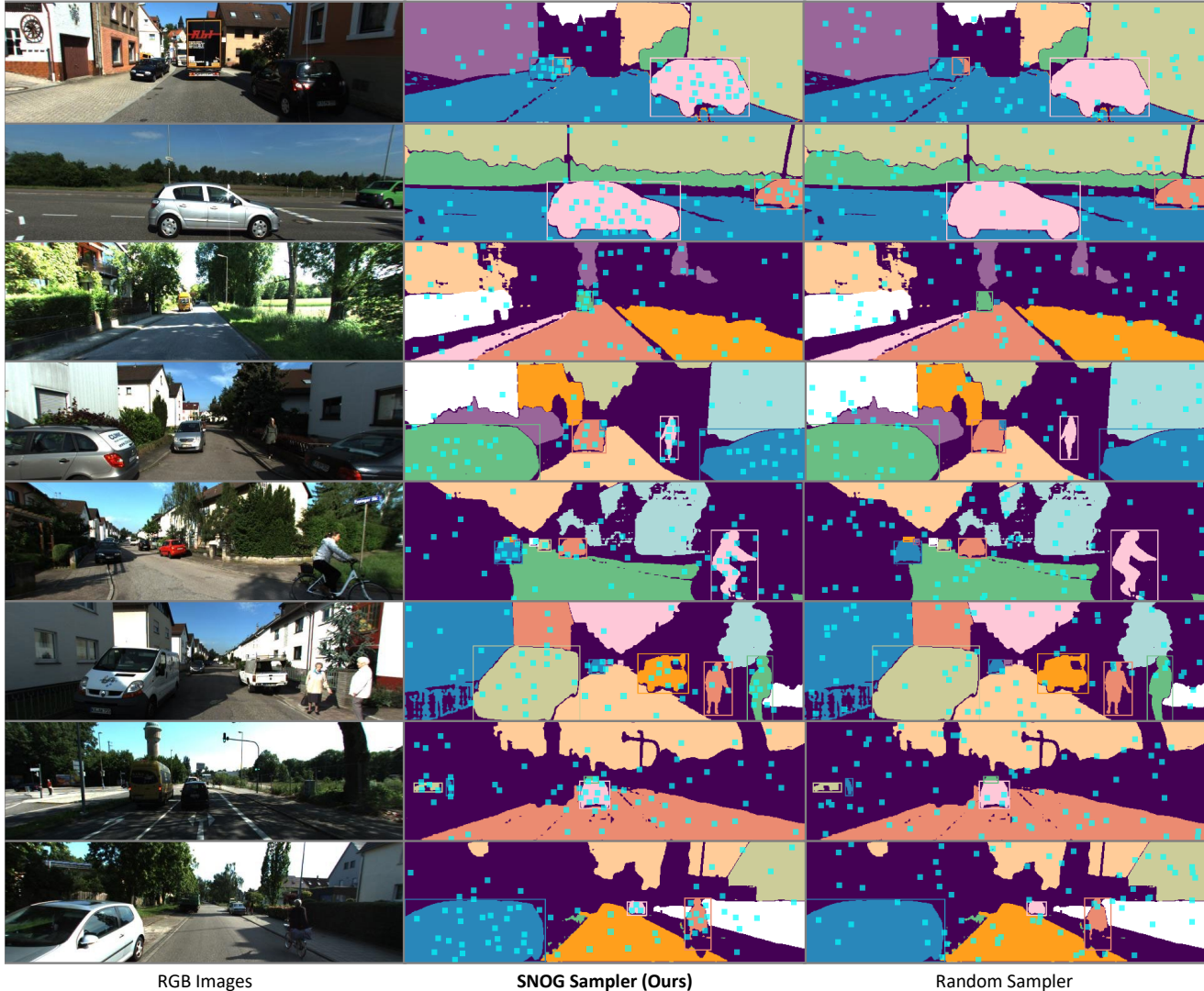


Figure 8. Comparison of sampled patches achieved using our proposed SNOG sampler and the random sampler.

where $\mathbf{r}_{i,j}$ denotes the i -th sampled ray during the j -th iteration, \mathcal{S} represents the set of rays associated with crucial instances, and T denotes the total number of iterations, which is set to 1,000 in our experiments.

Furthermore, we define ψ_v as the average proportion of valid rays sampled at crucial instances versus the total number of valid rays, which is expressed as follows:

$$\psi_v = \frac{1}{T} \sum_{j=1}^{j=T} \frac{|\{\mathbf{r}_{i,j} | \mathbf{r}_{i,j} \in \mathcal{S}_j\}|}{|\{\mathbf{r}_{i,j}\}|} \times 100\%. \quad (\text{A.6})$$

As illustrated in Table 10 and Fig. 8, our proposed SNOG sampler not only achieves significant improvements in both N_v and ψ_v but also produces much more plausible sampled patches compared to the random sampler used by previous SoTA methods [18, 32]. Our SNOG sampler can also be

Ray Sampler	$N_v (\times 10^3)$	$\psi_v (\%)$
Random Sampler	3.89	7.17
SNOG Sampler (Ours)	4.10	36.83
Improvement	5.40%	413.67%

Table 10. Efficiency comparison between random sampler and our proposed SNOG sampler.

embedded into other SoTA methods to improve their 3D scene reconstruction performance. As shown in Table 11, both BTS [32] and KYN [18] exhibit performance improvements when integrated with the SNOG sampler, primarily due to its instance-aware capabilities.

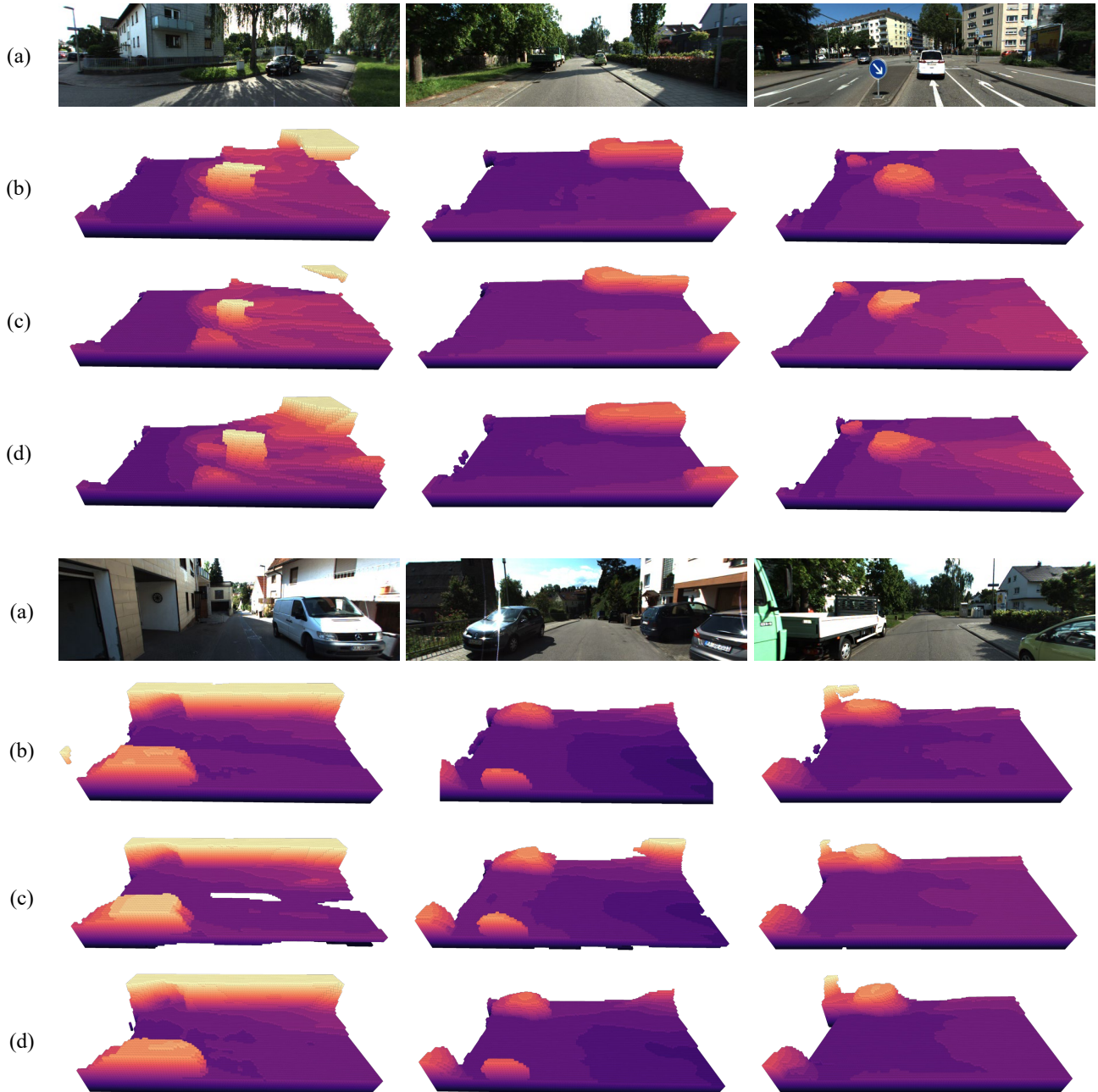


Figure 9. Comparison of 3D occupancy prediction on the KITTI-360 dataset: (a) input RGB images; (b) BTS [32] results; (c) KYN [18] results; (d) our results.

C.3. 3D Occupancy Prediction

We present additional qualitative experimental results of 3D occupancy prediction on the KITTI-360 dataset [19]. As illustrated in Fig. 9, our method demonstrates the following advantages compared to previous SoTA methods: 1) superior object reconstruction performance in distant areas (shown in the first four rows), primarily due to the instance-

aware sampling ray strategy in our proposed SNOG sampler; 2) fewer errors in 3D scene geometry recovery (shown in the last four rows), which can be attributed to the effective use of depth priors from the VFM and the enforcement of a reconstruction consistency constraint.

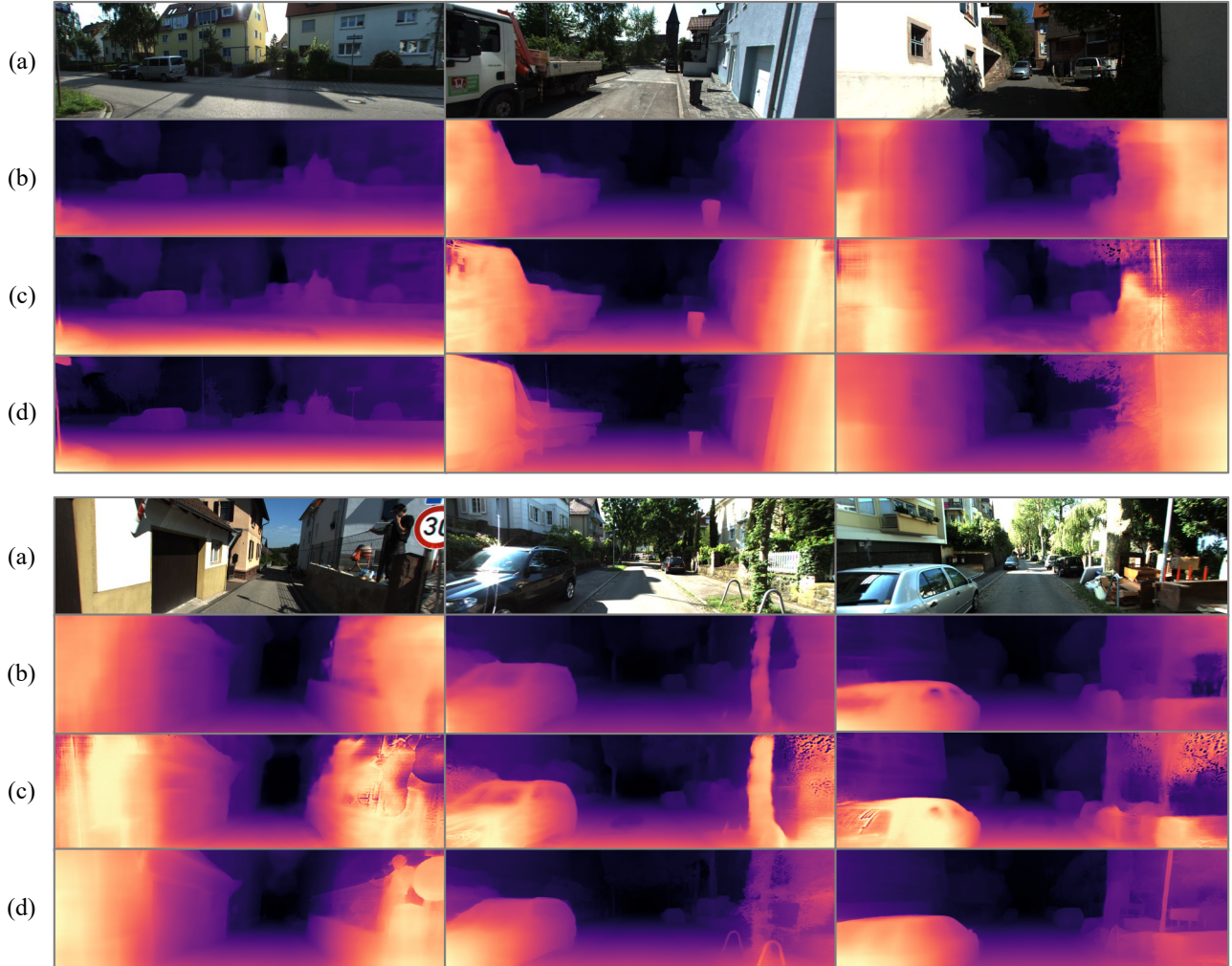


Figure 10. Comparison of metric depth estimation on the KITTI-360 dataset: (a) input RGB images; (b) BTS [32] results; (c) KYN [18] results; (d) our results.

Ray Sampler	BTS			KYN		
	O_{acc}^s	IE_{acc}^s	IE_{rec}^s	O_{acc}^s	IE_{acc}^s	IE_{rec}^s
w/o SNOG	0.91	0.65	0.64	0.92	0.70	0.66
w/ SNOG	0.92	0.65	0.65	0.92	0.70	0.67

Table 11. Comparison between previous SoTA methods with and without our proposed SNOG sampler embedded.

C.4. Metric Depth Estimation

We present additional qualitative experimental results of metric depth estimation on the KITTI-360 dataset [19]. As illustrated in Fig. 10, ViPOcc produces clearer boundaries of objects, such as trees, poles, and pedestrians, compared to previous SoTA methods BTS [32] and KYN [18]. In ad-

dition, our method demonstrates superior depth consistency in continuous regions, evident in vehicle glass and road surfaces. These improvements are attributed to the efficacy of our proposed inverse depth alignment module, which not only effectively eliminates domain discrepancies but also preserves the fine-grained depth priors from the VFM.